

1        **Assessing global-scale organic matter reactivity patterns in marine**  
2                    **sediments using a lognormal reactive continuum model**

3                    **Sinan Xu<sup>1,2,3</sup>, Bo Liu<sup>3</sup>, Sandra Arndt<sup>4</sup>, Sabine Kasten<sup>3,5</sup>, and Zijun Wu<sup>1\*</sup>**

4        <sup>1</sup>State Key Laboratory of Marine Geology, School of Ocean and Earth Science, Tongji  
5        University, Shanghai, 200092, China

6        <sup>2</sup>The Key Laboratory of Gas Hydrate, Ministry of Natural Resources, Qingdao Institute of  
7        Marine Geology, Qingdao, 266071, China

8        <sup>3</sup>Alfred Wegener Institute Helmholtz Centre for Polar and Marine Research, 27570  
9        Bremerhaven, Germany

10        <sup>4</sup>Department of Geosciences, Environment and Society, Universit´e Libre de Bruxelles,  
11        Avenue Franklin Roosevelt 50, 1050 Brussels, Belgium

12        <sup>5</sup>Faculty of Geosciences, University of Bremen, 28359 Bremen, Germany

13

14        **Correspondence to: Zijun Wu (wuzj@tongji.edu.cn)**

15

16        **Abstract**

17        Organic matter (OM) degradation in marine sediments is largely controlled by its  
18        reactivity and profoundly affects the global carbon cycle. Yet, there is currently no general  
19        framework that can constrain OM reactivity on a global scale. In this study, we propose a  
20        reactive continuum model based on a lognormal distribution (*l*-RCM), where OM  
21        reactivity is fully described by parameters  $\mu$  (the mean reactivity of the initial OM bulk  
22        mixture) and  $\sigma$  (the variance of OM components around the mean reactivity). We use the  
23        *l*-RCM to inversely determine  $\mu$  and  $\sigma$  at 123 sites across the global ocean. The results show

24 that the apparent OM reactivity ( $\langle k \rangle = \mu \cdot \exp(\sigma^2/2)$ ) decreases with decreasing  
25 sedimentation rate ( $\omega$ ) and show that OM reactivity is more than three orders of magnitude  
26 higher in shelf than that in abyssal regions. Despite the general global trends, higher than  
27 expected OM reactivity is observed in certain ocean regions characterized by great water  
28 depth and/or pronounced oxygen minimum zones, such as the Eastern-Western Coastal  
29 Equatorial Pacific and the Arabian Sea, emphasizing the complex control of the  
30 depositional environment (e.g., OM flux, oxygen content in the water column) on benthic  
31 OM reactivity. Notably, the *l*-RCM can also highlight the variability of OM reactivity in  
32 these regions. Based on inverse modeling results in our dataset, we establish the significant  
33 statistical relationships between  $\langle k \rangle$  and  $\omega$ , and further map the global OM reactivity  
34 distribution. The novelty of this study lies in its unifying view, but also in contributing a  
35 new framework that allows predicting OM reactivity in data-poor areas based on readily  
36 available (or more easily obtainable) information. Such a framework is currently lacking  
37 and limits our abilities to constrain OM reactivity in global biogeochemical and/or Earth  
38 System Models.

39

## 40 **1 Introduction**

41 Marine sediments act as the ultimate sink for organic carbon. The size and reactivity of  
42 the benthic organic matter (OM) reservoir is a critical component of the global carbon cycle  
43 (Arndt et al., 2013). In particular, the reactivity of benthic OM imposes a substantial control  
44 on the magnitude of benthic carbon burial over geological timescales due to the recycling  
45 of organic carbon by dissimilatory microbial activity in the deep biosphere (Boudreau,  
46 1992; Zonneveld et al., 2010), the dissolution and precipitation of carbonates (Meister et

47 al., 2022; Nöthen and Kasten, 2011), and the production of methane (Dickens et al., 2004;  
48 Whitticar, 1999). Decades of research have shown that OM reactivity is controlled by both  
49 the nature of the OM (origin, composition and degradation state), as well as its  
50 environmental and depositional conditions (e.g., redox conditions, sedimentation rate,  
51 mineral protection, microbial community composition and biological mixing) (Burdige,  
52 2007; Egger et al., 2018; Hartnett et al., 1998; Hedges and Keil, 1995; Larowe et al., 2020a;  
53 Zonneveld et al., 2010). However, due to the complex and dynamic nature of the main  
54 controls on OM reactivity, the specific relative significance of these controlling factors  
55 remains poorly quantified. Consequently, OM degradation models generally do not  
56 explicitly describe the influence of environmental and depositional factors on OM  
57 reactivity and its evolution but rather apply simplified parametrizations (Freitas et al., 2021;  
58 Pika et al., 2021). Over the past decades, several models have been developed and  
59 successfully used to quantify OM degradation in marine sediments. They can be broadly  
60 divided into two groups: discrete models, such as the (multi) *G* model (Bernier, 1964;  
61 Jørgensen, 1978), and continuum models, such as the reactive continuum model (RCM)  
62 (Boudreau and Ruddick, 1991) and the power model (Middelburg, 1989).

63 Discrete models divide the bulk OM pool into several discrete fractions, each with its  
64 own constant reactivity (Fig.1A). The 1-*G* model is the earliest OM degradation model,  
65 which is based on the assumption that OM degrades according to first order dynamics with  
66 a single constant degradation rate constant (Bernier, 1964). The multi-*G* model, however,  
67 divides OM into several fractions, and each fraction is degraded according to a first-order  
68 rate with a fraction-specific reactivity (Jørgensen, 1978). Although multi-*G* models  
69 successfully fit observed OM degradation dynamics when comprehensive data sets are

70 available, their application on a global scale is complicated by the need to partition the OM  
71 reactivity into a finite number of fractions and define their reactivities. A multi- $G$  model  
72 with  $n$  discrete OM fractions requires constraining  $2n-1$  parameters and is, thus, over-  
73 parametrized (Jørgensen, 1978). Nevertheless, because of its mathematical simplicity and  
74 wide use, multi- $G$  models have been used in a range of diagenetic models designed for the  
75 global/regional scale (e.g., CANDI, MEDIA, MEDUSA, and OMEN SED) (Boudreau,  
76 1996; Meysman et al., 2003; Munhoven, 2007; Pika et al., 2021). Constraining the  $2n-1$   
77 OM degradation model parameters for these global-scale applications is not  
78 straightforward. Early strategies for constraining the reactivity of OM on a global scale  
79 have focused on deriving empirical relationships between OM reactivity and single, easily  
80 observable characteristics of the depositional environment (water depth, sedimentation  
81 rate, or OM flux) (Arndt et al., 2013). However, poor statistically significant link between  
82 OM reactivity and depositional environment could be established ( $R^2 < 0.1$ ) after compiling  
83 published multi- $G$  model's parameters across a wide range of depositional environments,  
84 model complexities as well sediment depths/ burial time scales (Arndt et al., 2013).

85 Reactive continuum models (RCMs) are an alternative to discrete models. They assume  
86 that OM compounds are continuously distributed over a wide range of reactivities. The  
87 degradation rate can be described as the sum of an infinite number of discrete fractions,  
88 each degraded according to first-order kinetics (Boudreau and Ruddick, 1991), as

89 
$$G(t) = \int_0^{\infty} G(0) \cdot g(k, 0) \cdot e^{-kt} dk \quad (1)$$

90 where  $G(t)$  is OM content at time  $t$ ,  $G(0)$  is OM content at the sediment-water interface  
91 (SWI),  $k$  is the first-order degradation rate constant, and  $g(k,0)$  is the initial reactivity  
92 distribution of OM at the SWI. The key to constructing an RCM is to select a continuum

93 distribution that describes the OM reactivity at the SWI (Fig. 1B). Considering the  $k$  value  
 94 in Eq. 1 must be greater than zero ( $k > 0$ ), some of the all-axial statistical distributions ( $x \in$   
 95  $(-\infty, +\infty)$ ) are not appropriate for constructing RCM (e.g., Normal distribution, Fig.1D<sub>1</sub>).  
 96 Boudreau and Ruddick. (1991), following Aris (1968) and Ho et al. (1987), proposed to  
 97 use a Gamma distribution ( $\gamma$ -RCM, Fig.1D<sub>2</sub>) due to its mathematical properties and its  
 98 ability to capture the observed dynamics:

$$99 \quad g(k, 0) = \frac{a^\nu \cdot k^{\nu-1} \cdot e^{-ak}}{\Gamma(\nu)} \quad (2)$$

100 where  $a$  is the average age of the OM at the SWI,  $\nu$  is the shape parameter, and  $\Gamma(\nu)$  is the  
 101 Gamma function. In addition, Middelburg. (1989) empirically derived a power law from a  
 102 large data compilation of measured OM reactivity (Fig.1C), which is mathematically  
 103 equivalent to the  $\gamma$ -RCM. The advantage of the continuum models over the discrete models  
 104 is that they merely require constraining two free parameters to capture the widely observed  
 105 continuous decrease in OM reactivity with degradation time/depth. Recently,  $\gamma$ -RCM has  
 106 been used to inversely determine the free  $\gamma$ -RCM parameters, and thus benthic OM  
 107 reactivity, from observed POC and sulfate depth profiles across a wide range of different  
 108 depositional environments (Freitas et al., 2021). Although results revealed broad global  
 109 patterns, no significant statistical relationship ( $R^2 < 0.46$ ) between the parameters ( $a$  and  $\nu$ )  
 110 of the  $\gamma$ -RCM (Arndt et al., 2013) and characteristics of the depositional environment could  
 111 be found, and constraining OM degradation model parameters on the global scale thus  
 112 remains difficult.

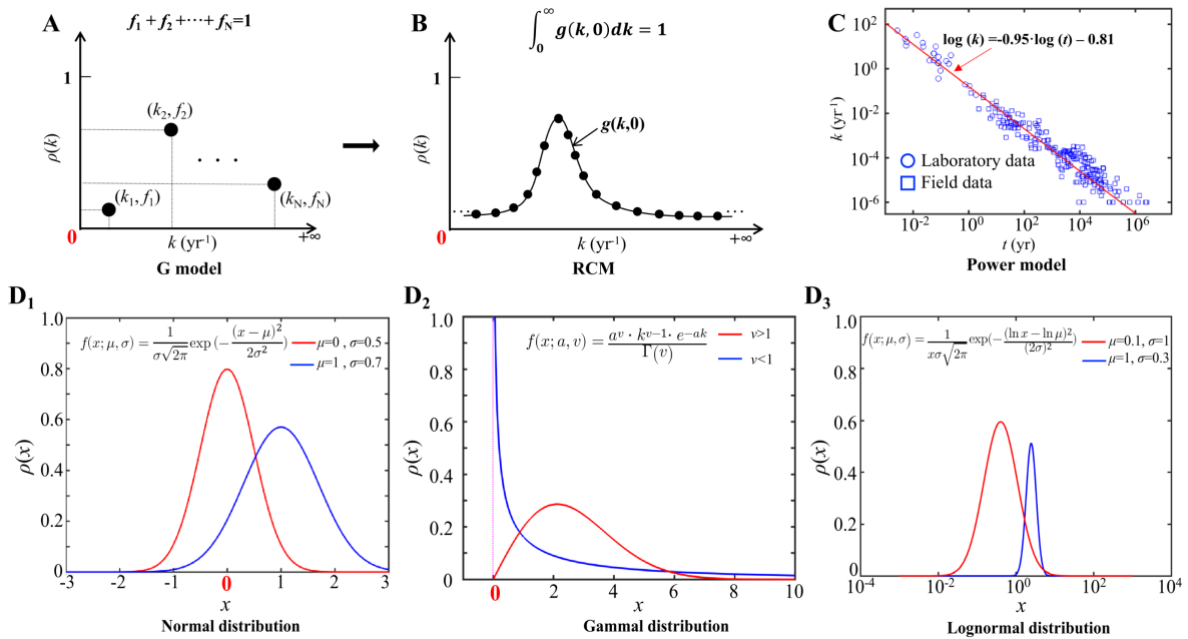
113 Here, we present an RCM based on a lognormal distribution (Forney and Rothman,  
 114 2012b):

$$115 \quad g(k, 0) = \frac{1}{k \cdot \sigma \cdot \sqrt{2\pi}} \cdot e^{-(\ln k - \ln \mu)^2 / (2\sigma^2)} \quad (3)$$

116 where  $\ln \mu$  is the mean of  $\ln k$ , and  $\sigma^2$  is the variance of  $\ln k$  (Fig.1D3). Parameter  $\mu$   
 117 determines the mean reactivity of the initial OM bulk mixture and parameter  $\sigma$  reflects the  
 118 spread of OM components around the mean reactivity.

119 The lognormal distribution is formed by the multiplicative effects of random variables,  
 120 which is commonly observed in nature (e.g., the radioactivity of elements in the crust, the  
 121 incubation period of infectious diseases, and ecological species abundance) (Limpert et al.,  
 122 2001). In the ocean system, the rates of ocean primary production and biological carbon  
 123 export also fit the lognormal distribution (Cael et al., 2018). The degradation of OM in  
 124 natural ecosystems is controlled by a network of biologically, physically, and chemically  
 125 driven processes (Forney and Rothman, 2014), so the variables raised from such  
 126 multiplicative processes are often followed by a lognormal distribution. Forney and  
 127 Rothman (2012b) showed that litter bag OM incubation data is indeed best described by a  
 128 lognormal distribution of rates.

129



130 **Figure 1. Schematic diagram of different OM degradation models.** A: G model, B:  
131 RCM, C: Power model and D: Common continuum distribution functions. The  $x$  coordinate  
132 denotes the variation range of values, and the  $y$  coordinate denotes the probability density  
133 distribution ( $\rho$ ) (D<sub>1</sub>: the Normal distribution, a typical all-axis distribution, D<sub>2</sub>: the Gamma  
134 distribution, a typical semi-axis ( $x>0$ ) distribution, and D<sub>3</sub>: the Lognormal distribution, a  
135 typical semi-axis ( $x>0$ ) distribution).

136

137 In this study, we first compared the  $l$ -RCM with other OM degradation models and  
138 analyzed the advantages of the  $l$ -RCM in describing the OM reactivity distribution. Then  
139 we simulated OM degradation in marine sediment at 123 global sites using the  $l$ -RCM.  
140 Based on inverse modeling results in our dataset, we established the empirical formulas of  
141 OM reactivity vs sedimentation rate and further mapped the global OM reactivity  
142 distribution. This study provides a new framework for assessing OM reactivity on  
143 regional/global scales and predicting OM reactivity in data-poor areas based on easily  
144 obtainable environmental parameters (e.g., sedimentation).

145

## 146 **2 Materials and methods**

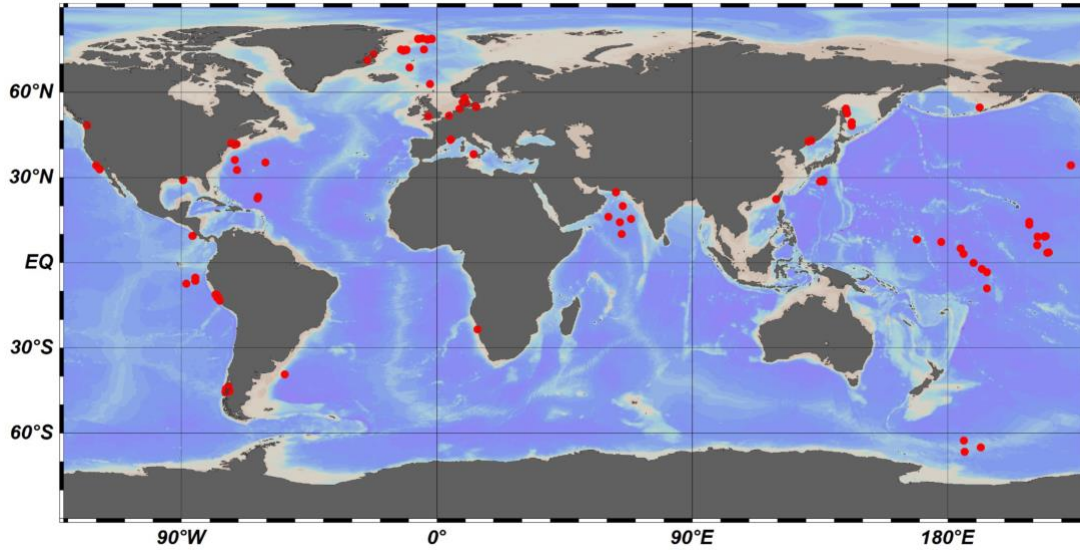
### 147 **2.1 OM degradation model approach**

148 We constructed an RCM with lognormal distribution ( $l$ -RCM) to simulate the OM  
149 degradation in marine sediments. The  $g(k,0)$  we used in Eq. 1 is the lognormal distribution  
150 (Eq.3). Because of the tail of  $g(k,0)$ , the mean rate constant for bulk OM degradation or the  
151 apparent degradation rate of the bulk OM ( $\langle k \rangle$ ) is written as follows:

$$152 \quad \langle k \rangle = \int_0^{\infty} k \cdot g(k, 0) dk = \mu \cdot e^{\sigma^2/2} \quad (4)$$

### 153 **2.2 Inverse model approach**

154 Here, we used 123 published datasets of OM depth profiles across a wide range of  
 155 different depositional environments that have been sourced from published literature  
 156 (Middelburg, 1989; Arndt et al., 2013; Middelburg et al., 1997) and the IODP database  
 157 (Fig.2, Supplementary Table S1) to inversely determine the  $\mu$  and  $\sigma$  parameters. We also  
 158 analyzed a small number ( $n=12$ ) of laboratory experiment data on OM degradation  
 159 (Middelburg, 1989), as well as OM degradation data ( $n=16$ ) from terrestrial soils (Katsev  
 160 and Crowe, 2015). We followed the inverse modeling approach by Forney et al.(2012a) to  
 161 identify the best-fitting parameters  $\mu$  and  $\sigma$  based on the Newton method.



162 **Figure 2. Global distribution of investigated sites.**

163  
 164  
 165 Notably, the burial time was correlated with the porosity. A simple exponential function  
 166 was used to describe porosity in sediments:

$$167 \quad \varphi(x) = \varphi_0 \cdot e^{-\lambda x} \quad (5)$$

168 where  $\varphi_0$  is the values of porosity at the SWI,  $\lambda$  is the attenuation coefficient, and  $x$  is  
 169 depth. Considering the compaction impacts on OM degradation, the burial time  
 170 corresponding to each depth in the OM profile can be calculated as:



171 
$$t(x) = \int_0^x \omega^{-1} dx = \frac{x}{\omega_f} + \frac{(\varphi_0 - \varphi_f)}{(1 - \varphi_f) \cdot \lambda \cdot \omega_f} \cdot (e^{-\lambda \cdot x} - 1) \quad (6)$$

172 where  $\varphi_f$  is the values of porosity at larger depths, calculated from Eq. 5 and the pre-set  
 173 simulation depth. If the porosity data were not available, the global set as: shelf regions  
 174 ( $\varphi_0$ : 0.45,  $\lambda$ :  $0.5 \times 10^{-3}$ ), slope regions ( $\varphi_0$ : 0.74,  $\lambda$ :  $1.7 \times 10^{-4}$ ), and abyssal regions ( $\varphi_0$ : 0.7,  $\lambda$ :  
 175  $0.85 \times 10^{-3}$ ) (LaRowe et al., 2020b).

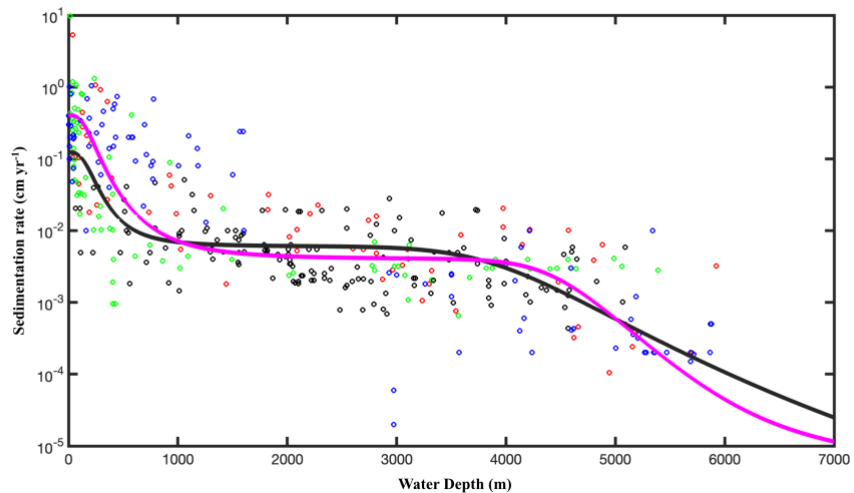
176 **2.3 Global upscaling of sedimentation rate**

177 The inversely determined  $\mu$ ,  $\sigma$  couples of all investigated sites were then used in a linear  
 178 regression method to derive the empirical relationships between OM parameters  $\mu$ ,  $\sigma$ ,  $\langle k \rangle$   
 179 and the local sedimentation rates ( $\omega$ ). A correction factor ( $f_c$ , Eq.7) was applied to calculate  
 180 the skewness bias inherent in the back conversion from a log-log transformed linear  
 181 regression model to arithmetic units (Egger et al., 2018; Middelburg et al., 1997).

182 
$$f_c = e^{2.65 \times s^2} \quad (7)$$

183 where  $s^2$  is the variance of the model residuals. The newly derived empirical  
 184 relationships between  $\langle k \rangle$  and  $\omega$  were then used to calculate global maps of OM reactivity  
 185 at the SWI on a  $1^\circ \times 1^\circ$  grid cell of the world ocean. At each grid point,  $\omega$  was estimated  
 186 based on the empirical relationship between  $\omega$  ( $\omega$  in  $\text{cm yr}^{-1}$ ) and the water depth ( $z$  in m)  
 187 (Eq.8, Fig.3), derived from 260 observations on the global continental shelves (Burwicz et  
 188 al., 2011), complemented here by an extra 360 sites including abyss regions (data from  
 189 Arndt et al. (2013), Egger et al. (2018)).

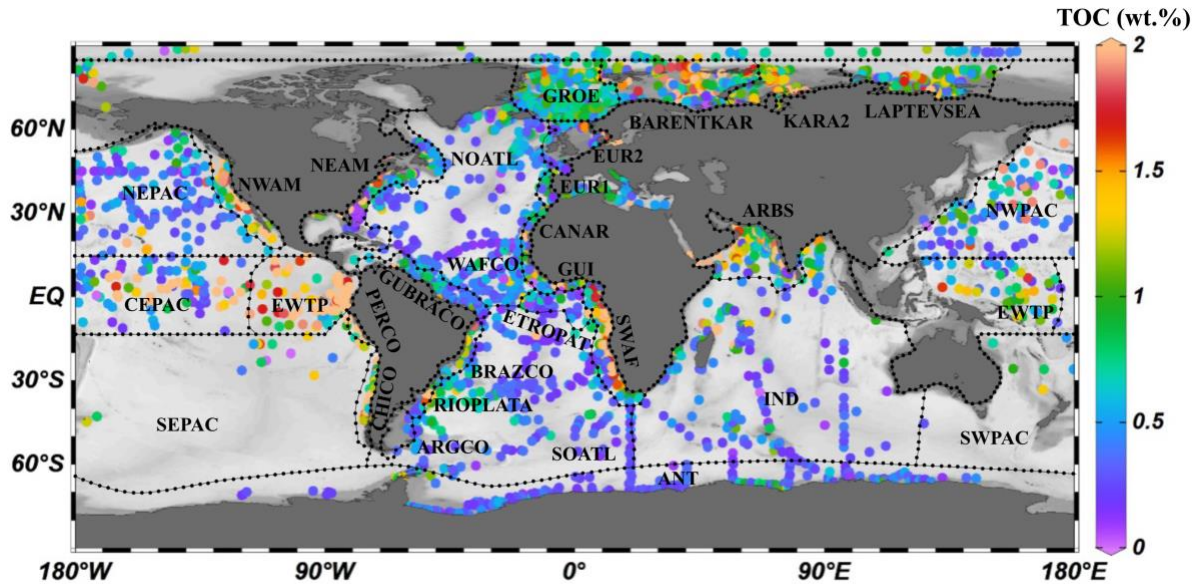
190 
$$\omega(z) = \frac{0.4}{1 + \left(\frac{z}{200}\right)^{3.5}} + \frac{0.004}{1 + \left(\frac{z}{4500}\right)^{17}} \quad (8)$$



191  
 192 **Figure 3. Relationship between Sedimentation rate ( $w$ ) and water depth ( $z$  in m).** The  
 193 data are taken from Arndt et al. (2013) (black circles), Egger et al.(2018) (pink circles),  
 194 Betts and Holland (1991) (red circles), Colman and Holland (2000) (green circles), and  
 195 Seiter et al. (2004) (blue circles). The pink line is the fitting result according to Eq. 8  
 196 ( $R^2=0.57$ ), and the black line is the fit obtained from the data of Burwicz et al. (2001)  
 197 ( $R^2=0.43$ ).

198

199 Considering the geographic differences in depositional environments and to describe the  
 200 global distribution of sedimentary OM reactivity in more detail, we divided the global  
 201 ocean into 30 different regions (Table 2, Fig.4) using 5600 single measured data of OM  
 202 content in global surface sediment (<5 cm sediment depth) and the previously used  
 203 combined qualitative and quantitative geostatistical methods (Seiter et al., 2004).



204

205 **Figure 4. The 30 different regions of the global ocean were divided using 5600 single**  
 206 **measured data of OM content (wt.%) of surface sediments**

207

### 208 **3 Results and discussion**

#### 209 **3.1 OM reactivity distribution described by the $\gamma$ -RCM and the $l$ -RCM**

210 To compare OM reactivity distribution described by the  $l$ -RCM and the  $\gamma$ -RCM, we  
 211 determined the best fit to the eight OM datasets reported by Boudreau and Ruddick. (1991).  
 212 The results show that both RCMs fit the data equally well, as illustrated by the high  
 213 coefficient of determination for each fit ( $R^2 > 0.9$ , Table 1 and Fig.5). However, the  $l$ -RCM  
 214 and the  $\gamma$ -RCM differ in their ability to find a unique solution and in their respective  
 215 probability density functions of OM reactivity ( $\rho(k)$ ). For example, Fig.6A and 6B show  
 216 the best-fit OM profiles for two contrasting sites: BX-6 on the shelf and DSDP 58 in the  
 217 abyssal region. The inversely determined parameters at the two sites are  $\mu = 2.23 \times 10^{-3} \text{ yr}^{-1}$ ,  
 218  $\sigma = 2.03$  at BX-6, and  $\mu = 6.11 \times 10^{-5} \text{ yr}^{-1}$ ,  $\sigma = 1.66$  at DSDP 58 by the  $l$ -RCM. At BX-6, the

219 best-fitting parameters by the  $\gamma$ -RCM are  $\nu = 0.278$  and  $a = 22.5$ , and at DSDP 58,  $\nu = 1.08$   
220 and  $a = 20224$ . According to the parameter sensitivity analysis, the  $R^2$  of the fitted results  
221 remains greater than 0.9 when  $a$  and  $\nu$  change substantially simultaneously (Fig.6D,  
222 Supplementary Table S2, Fig.S1, S2, and S3). As a result, different combinations of  $a$  and  
223  $\nu$  can fit the data equally well. For example, simultaneously increasing  $\nu$  and  $a$  ( $\nu = 0.5$  and  
224  $a = 53$ ) at site BX-6 or decreasing  $\nu$  and  $a$  ( $\nu = 0.5$  and  $a = 4024$ ) at site DSDP 58 lead to a  
225 slight change in  $R^2$ . Adding additional measured data, such as depth profiles of porewater  
226 sulfate and methane concentrations, can help find a unique solution (Freitas et al., 2021).  
227 In contrast, the best-fit parameters  $\mu$  and  $\sigma$  are unique in the  $l$ -RCM, and even small changes  
228 in either parameter can lead to abysmal fitting results (Fig.6D). The second difference  
229 between the two models concerns the shape of the probability distribution  $\rho(k)$ .  
230 Statistically, the features of the Gamma distribution vary with the value of  $\nu$ . If  $\nu < 1$ ,  $\rho(k)$   
231 tends to positive infinity when  $k$  approaches zero. In contrast, if  $\nu > 1$ ,  $\rho(k)$  tends to zero  
232 when  $k$  approaches zero. Hence, the characteristics of the Gamma distribution under  
233 different  $\nu$  values are difficult to visually compare the OM reactivity distributions at site  
234 BX-6 ( $\nu < 1$ ) and DSDP 58 ( $\nu > 1$ ) (Fig.6C). Compared with  $\gamma$ -RCM, the  $l$ -RCM can better  
235 distinguish OM reactivity distribution at different sites.

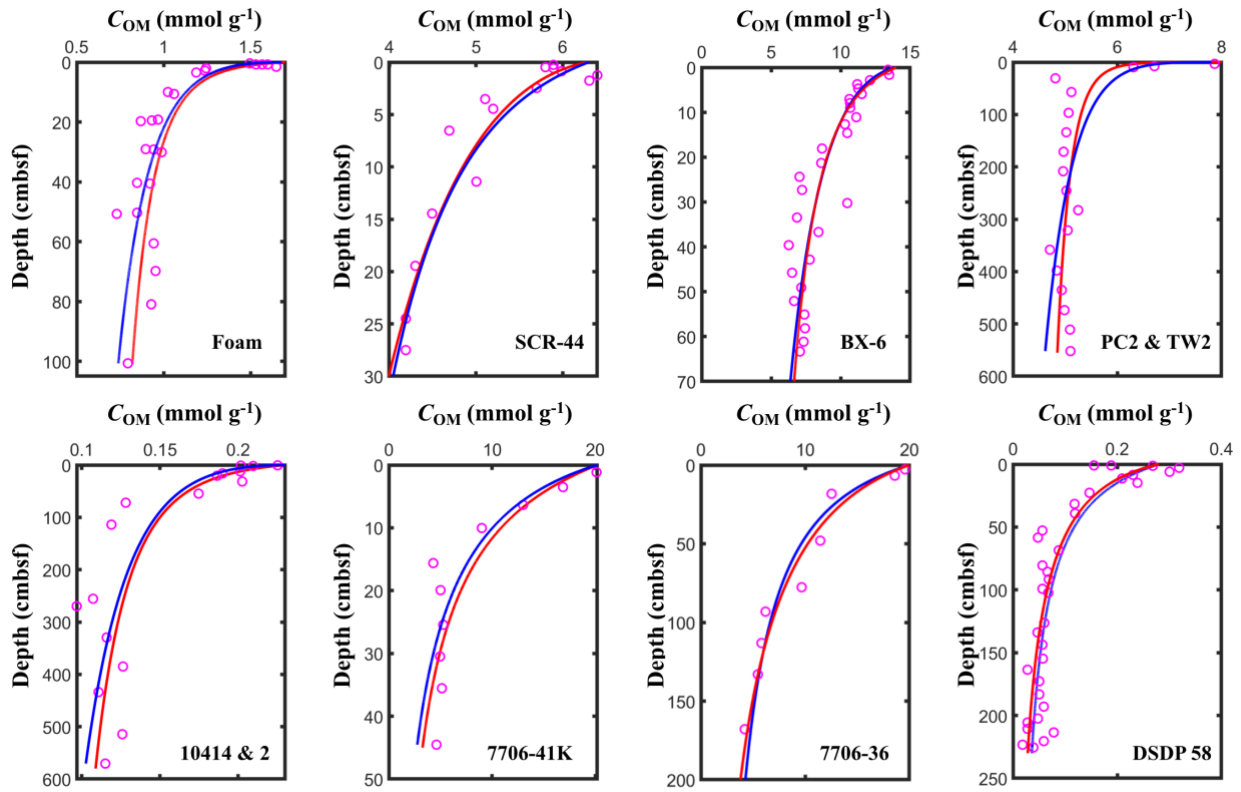
236

237 **Table 1. List of model parameters and coefficients of determination ( $R^2$ ) for the**  
238 **fitting result of  $\gamma$ -RCM and  $l$ -RCM.**

Core	$\gamma$ -RCM			$l$ -RCM		
	$\nu$ (-)	$a$ (yr)	$R^2$	$\mu$ (yr <sup>-1</sup> )	$\sigma$ (-)	$R^2$
Foam	0.152	4.2	0.930	$2.2 \times 10^{-3}$	3.725	0.923
SCR-44	0.202	70.4	0.929	$4.4 \times 10^{-4}$	2.706	0.922
BX-6	0.278	22.5	0.929	$2.24 \times 10^{-3}$	2.031	0.936
PC2&TW2	0.052	0.16	0.937	$5.5 \times 10^{-5}$	6.688	0.947
10141&2	0.193	10184	0.935	$1.9 \times 10^{-6}$	3.289	0.936
7706-41K	0.910	141.3	0.974	$9.5 \times 10^{-3}$	0.899	0.972

<b>7706-36</b>	0.804	231.7	0.978	$4.79 \times 10^{-4}$	1.089	0.980
<b>DSDP58</b>	1.080	20224	0.917	$6.11 \times 10^{-5}$	1.663	0.921

239



240

241

**Figure 5. Fitting results of the  $l$ -RCM and the  $\gamma$ -RCM.** The pink dots are the measured

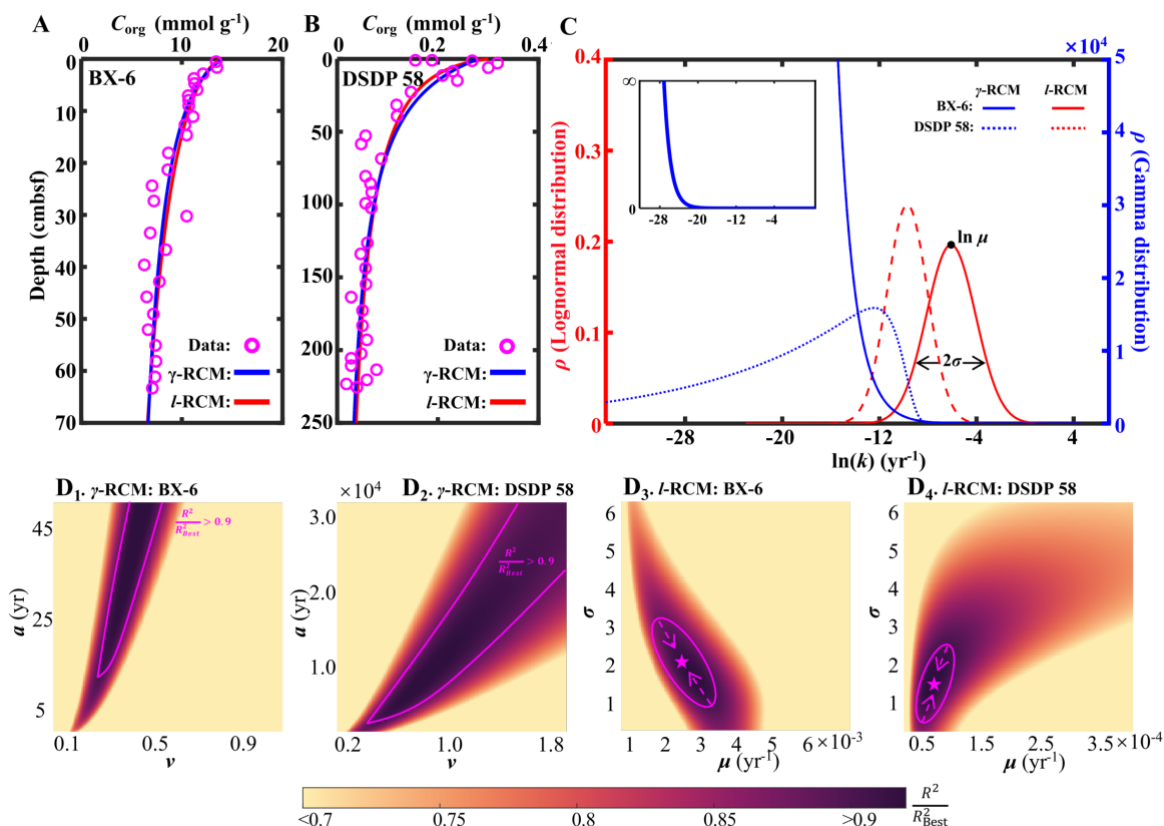
242

OM data, the red lines are  $l$ -RCM fitting results, and the blue lines are  $\gamma$ -RCM fitting

243

results.

244



245

246 **Figure 6. Comparison of  $l$ -RCM and  $\gamma$ -RCM.** A, B: the fitting results of the  $l$ -RCM and  
 247 the  $\gamma$ -RCM for site BX-6 and DSDP 58. C: OM reactivity distribution from  $l$ -RCM and  $\gamma$ -  
 248 RCM. Top inset, Gamma distribution at site BX-6 at a larger y-axis. D: Distribution of  
 249  $R^2/R_{\text{Best}}^2$  for parameter sensitivity analysis of the  $\gamma$ -RCM and the  $l$ -RCM at sites BX-6 and  
 250 DSDP 58. The pink lines in the D<sub>1</sub> and D<sub>2</sub> denote the range that  $R^2/R_{\text{Best}}^2 > 0.9$  in the  $\gamma$ -RCM.  
 251 The  $R^2/R_{\text{Best}}^2$  in the  $l$ -RCM converges as the pink arrows in the D<sub>3</sub> and D<sub>4</sub>, ultimately  
 252 reaching the best fitting results as the pink pentagrams.

253

### 254 3.2 Regional distribution of OM reactivity

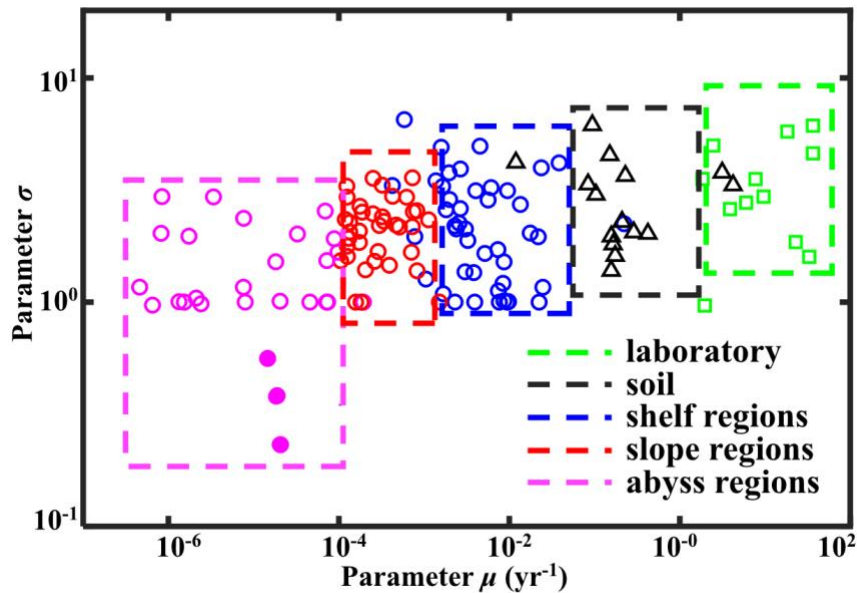
255 In the  $l$ -RCM, parameter  $\mu$  represents the mean reactivity of the OM fractions, which  
 256 dominates the rate of OM degradation (Supplementary Fig.S2), and parameter  $\sigma$  describes  
 257 the homogeneity of OM fractions, with larger  $\sigma$  value indicating more heterogeneous  
 258 mixture of OM (Forney et al., 2012b). The inverse determination of the  $l$ -RCM parameters

259  $\mu$  and  $\sigma$  across the wide range of different depositional environments allows quantitative  
260 insights into OM reactivity and provides essential information on the main environmental  
261 controls on OM reactivity. Fig.7 illustrates the inversely determined  $\mu$ - $\sigma$  for all 123 depth  
262 profiles of marine sediment POC investigated in this study and compares them with  
263 inversely determined parameters from published soil and laboratory incubation data. It  
264 highlights the large inter- and intraregional variability of best-fit  $\mu$  ( $10^{-6}$ – $10^2$  yr<sup>-1</sup>) and  $\sigma$   
265 (0.2–6). However, despite the large variability, it also reveals broad global patterns in  $\mu$   
266 and  $\sigma$ . Notably, best-fit  $\mu$ - $\sigma$  couples form environmental clusters along a  $\mu$  gradient, with  
267 the highest  $\mu$  being determined for laboratory degradation experiments of fresh  
268 phytoplankton (Garber, 1984; Westrich and Berner, 1984) ( $\mu=10^0$ – $10^2$  yr<sup>-1</sup>), followed by  
269 soil incubation under natural (Katsev and Crowe, 2015), yet still idealized conditions  
270 ( $\mu=10^0$ – $10^1$  yr<sup>-1</sup>), while OM degraded in marine sediments generally reveals lower  
271 inversely determined  $\mu < 10^0$  yr<sup>-1</sup>. The higher  $\mu$  values determined for soil OM seemingly  
272 contradict the widely accepted notion that soil OM is generally less reactive than marine  
273 OM (Larowe et al., 2020a; Zonneveld et al., 2010). However, this apparent contradiction  
274 can be explained by the idealized conditions of the incubation experiments (e.g., only one  
275 type of material, some of which had nitrogen added), as well as the degradation state of the  
276 investigated OM. Although soil OM is structurally less reactive (Hedges and Keil, 1995;  
277 Zonneveld et al., 2010), the soil incubation experiments were conducted with initially  
278 undegraded material. In contrast, OM deposited in marine sediments consists of a complex  
279 mixture of OM from autochthonous and allochthonous sources that is altered to various  
280 degrees during transit from its source to the sediment (Hewson et al., 2012).

281 In addition to the difference between incubation data and field observations, Fig.7 also  
282 reveals a three order of magnitude decrease in inversely determined  $\mu$  for OM from the  
283 shelf ( $10^{-3}$ – $10^{-1}$  yr<sup>-1</sup>) to the slope ( $10^{-4}$ – $10^{-3}$  yr<sup>-1</sup>), and ultimately abyssal regions ( $<10^{-4}$  yr<sup>-1</sup>).  
284 In addition, shelf and slope regions also generally reveal a larger  $\sigma$  (1–3), while abyssal  
285 regions display a narrower  $\sigma$  range (0.5–1). This observed progressive decrease in  $\mu$  and  $\sigma$   
286 from the shelf to the abyssal ocean confirms previously observed patterns (Arndt et al.,  
287 2013; Freitas et al., 2021; Zonneveld et al., 2010) and reflects the interaction between OM  
288 structure (or its source) and the degree of alteration/pre-processing as OM transits from its  
289 original source to the ultimate sedimentary sink. In the dynamic shelf regions, highly  
290 variable OM loads from different sources, including *in-situ* produced marine OM, laterally  
291 transported, pre-processed terrestrial or marine OM, are often physically protected from  
292 further erosion/deposition cycles due to high suspended sediment loads (Arndt et al., 2013;  
293 Larowe et al., 2020a). As a result, benthic OM is composed of a complex mixture of fresh  
294 and pre-aged compounds of highly variable (hence larger  $\sigma$  of the initial distribution), yet  
295 generally higher reactivity. On the upper and mid-continental slopes, intensive lateral  
296 and/or vertical transport processes or the abrupt relocation of sediment result in similar  
297 complex mixtures of OM (hence similar  $\sigma$  of the initial distribution) (Larowe et al., 2020a).  
298 However, transport timescales are often longer due to the greater water depths and distance  
299 to land. The deposited OM is generally more degraded and thus less reactive than in shelf  
300 environments. In contrast, benthic OM in abyssal regions is mainly derived from marine  
301 production (Rowe and Staresinic, 1979; Larowe et al., 2020a). During its slow settling  
302 through the water column, highly reactive OM compounds are rapidly degraded, and only  
303 the less reactive compounds persist and settle onto the sediment (Dunne et al., 2007). The



304 values of  $\mu$  and  $\sigma$  in the abyssal regions are thus significantly smaller than in the shelf and  
 305 slope regions. The decrease of  $\mu$  and  $\sigma$  from the shelf to abyssal regions reveals a decline  
 306 in reactivity during lateral transport of OM, where  $\mu$  mainly controls the overall reactivity  
 307 and  $\sigma$  indicates the coverage of the main component of OM.



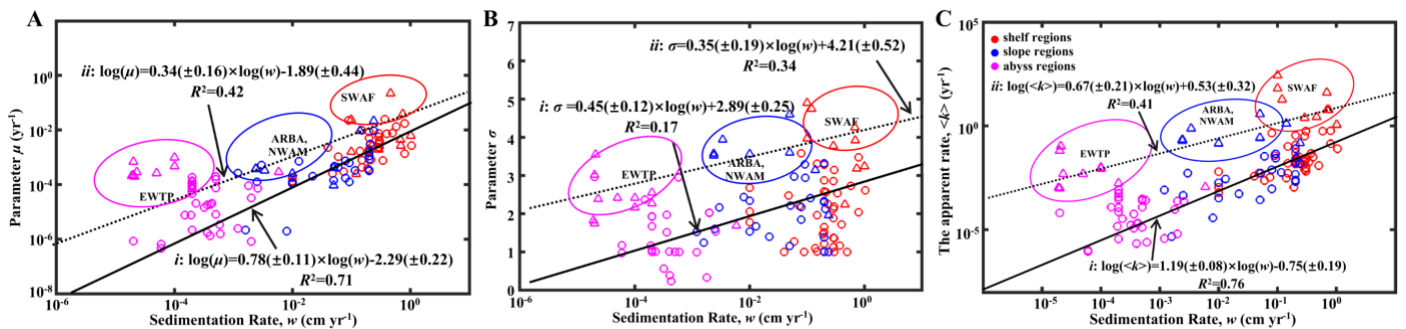
308  
 309 **Figure 7. Regional distribution of OM reactivity.** Distribution of parameters  $\sigma$  and  $\mu$  in  
 310 different regions. Pink solid circles denote fitting results of sites in the NEPAC with  
 311 extremely low OM reactivity.

### 313 3.3 Global distribution patterns of OM reactivity

314 Parameters  $\mu$  and  $\sigma$  together control the degradation process of OM, which can be further  
 315 described by the apparent degradation rate of the bulk OM ( $\langle k \rangle$ ). Sedimentation rate ( $\omega$ )  
 316 is a widely observed and comparably easy to measure proxy for local depositional  
 317 conditions with sizable global data sets or empirical formulas available (Burwicz et al.,  
 318 2011). Fig. 8A, 8B and 8C show the global decreasing trend of  $\mu$ ,  $\sigma$  and  $\langle k \rangle$  with  $\omega$  for the  
 319 general sea regions (shelf (<200m), slope (200–2000m), and abyss (>2000m)). The active

320 OM fractions (e.g., sugars and proteins) are preferentially exhausted during the lateral  
321 transport of OM from the shelf to the abyssal regions, leading to a decrease in the mean  
322 OM reactivity ( $\mu$ , Fig. 8A), and thus OM is mainly composed of refractory components ( $\sigma$ ,  
323 Fig. 8B). Due to the multiple sources of OM in the shelf regions, including fresh and older  
324 OM imported laterally by inland rivers, and OM settled from the euphotic layer (LaRowe  
325 et al., 2020a), the values of the values of  $\mu$ ,  $\sigma$  and  $\langle k \rangle$  fluctuates significantly. However,  
326 the general trend is superimposed by a large variability and apparent reactivity  $\langle k \rangle$  in  
327 specific environments, notably deviating from this generally observed trend. More  
328 specifically, higher  $\mu$  and  $\sigma$  values and, thus, higher OM reactivities occur in the Eastern-  
329 Western Coastal Equatorial Pacific (EWEP), Southwestern-Africa continental margin  
330 (SWAF), Northwestern-America continental margin (NWAM), and the Arabian Sea  
331 (ARBS) regions. These results are completely consistent with prior observations and model  
332 results (Arndt et al., 2013) and can be directly linked to the prevailing water-column redox  
333 and depositional conditions. High benthic OM reactivities have previously been reported  
334 for depositional environments that are characterized by a dominance of marine algal OM  
335 (Hammond et al., 1996) and strong lateral transport processes (e.g., SWAF, NWAM)  
336 (Arndt et al., 2013). Consequently, the larger values of all  $\mu$  and  $\sigma$ , and  $\langle k \rangle$  occur in the  
337 inverse modelling results for these depositional environments (Fig. 8). Furthermore, the  
338 reactivity of sedimentary OM is considerably influenced by oxygen content or more  
339 precisely, by oxygen exposure time in the water column and at the seafloor (Aller, 1994;  
340 Hartnett et al., 1998; Hedges and Keil, 1995; Mollenhauer et al., 2003; Zonneveld et al.,  
341 2010). Lower oxygen concentrations, as present in these regions in the form of pronounced  
342 oxygen minimum zones (OMZs), will slow down the degradation of OM both in the water

343 column and at the sediment surface (Jørgensen et al., 2022). This enables the burial of more  
 344 reactive OM into the sediments and thus results in the occurrence of high sedimentary OM  
 345 reactivity in these regions despite great water depth (e.g., ARBS, EWTP) (Arndt et al.,  
 346 2013; Bogus et al., 2012; Ingole et al., 2010; Luff et al., 2000; Volz et al., 2018). The *l*-  
 347 RCM not only captures the broad patterns of OM reactivity across the global seafloor even  
 348 better than previous models, but also provides statistically more significant relationships  
 349 between OM reactivity ( $\langle k \rangle$ ) and sedimentation rate ( $\omega$ ) than inversely determined  
 350 parameters of  $\gamma$ -RCM ( $R^2 < 0.46$ ) and discrete models ( $R^2 < 0.1$ ) (Arndt et al., 2013).  
 351 Considering that no robust quantitative framework exists at this stage to predict OM  
 352 reactivity as a function of easily observable environmental parameters, the *l*-RCM provides  
 353 an excellent first-order predictor and a step forward in assessing the global distribution  
 354 patterns of OM reactivity, despite the poor relationship between  $\langle k \rangle$  and  $\omega$  for these special  
 355 regions (e.g., EWEP, SWAF, NWAM, and ARBS).



357 **Figure 8. Global distribution patterns of OM reactivity.** A. Log-log plot of  $\omega$  and  $\mu$ . B.  
 358 Log-log plot of  $\omega$  and  $\sigma$ . C. Log-log plot of  $\omega$  and  $\langle k \rangle$ . The solid black line (i) denotes  
 359 linear regression for shelf, slope, and abyssal regions. The black dotted line (ii) denotes  
 360 linear regression for high OM reactivity regions, including the EWTP, ARBS, NWAM,  
 361 and SWAF regions.

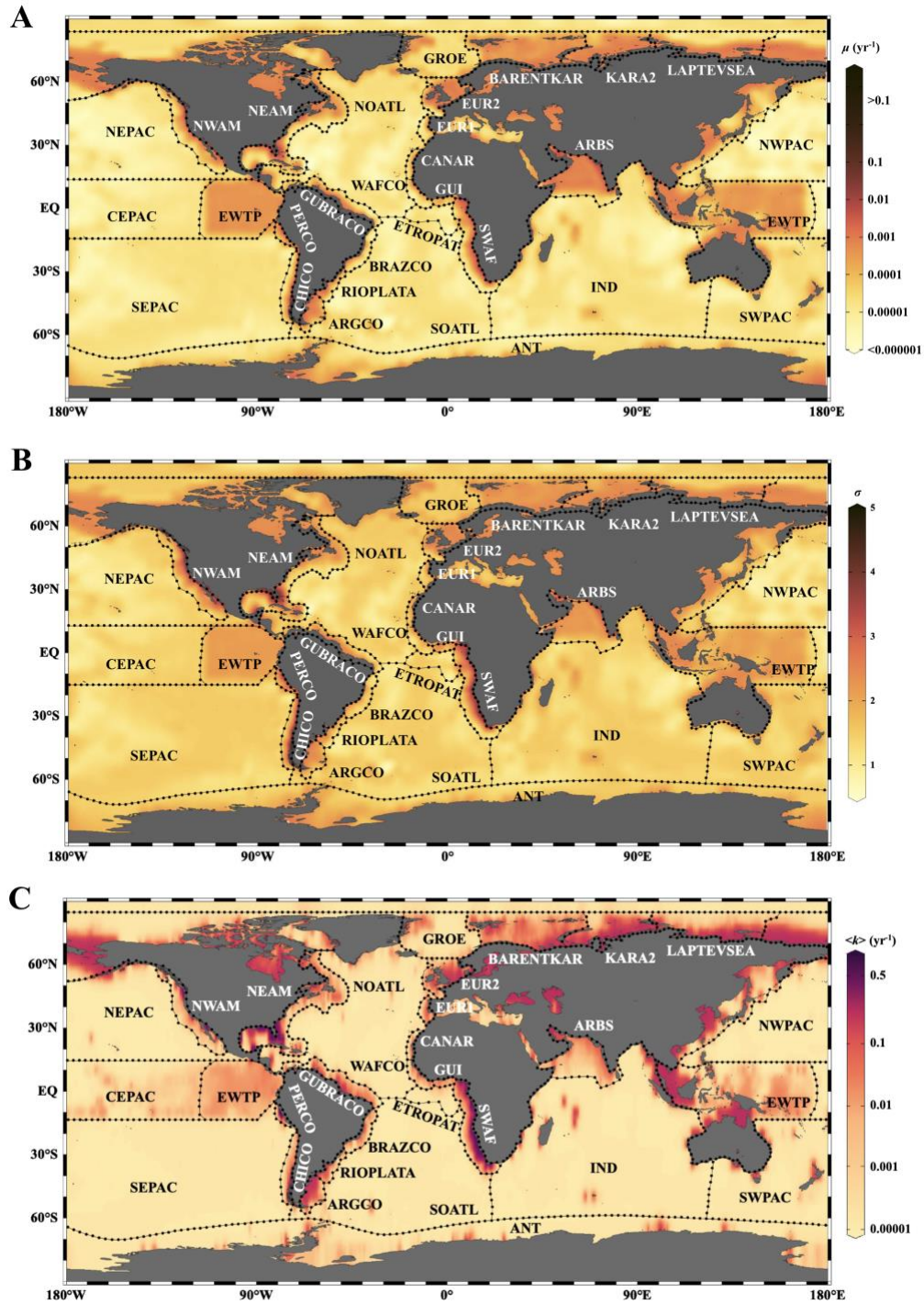
362

363 Based on the empirical relationships in Fig.8 (*i* for the general water depth-related  
364 regions, *ii* for the specific regions (EWTP, ARBS, NWAM, and SWAF)), and the water  
365 depth– $\omega$  relationship (Eq.8), we finally derived, to our knowledge, the world’s first map  
366 of the global distribution of parameter  $\mu$ ,  $\sigma$ , and  $\langle k \rangle$  (Fig.9). Using the relationship between  
367 water depth,  $\omega$ , and  $\langle k \rangle$  (Fig.3 and Fig.8C), we further estimated the mean apparent OM  
368 reactivity ( $\langle K_{\text{region}} \rangle$ ) in the 30 regions of global ocean (Table 2). Furthermore, the  
369 heterogeneity of the OM reactivity distribution in global marine sediments is well  
370 illustrated in Fig. 9. Specifically, higher  $\mu$  (Fig.9A),  $\sigma$  (Fig.9B), and OM reactivity (Fig.9C)  
371 is reflected in shelf regions, particularly in northern Atlantic provinces with high latitudes  
372 (e.g., Barents Sea ( $\langle K_{\text{region}} \rangle \approx 0.02 \text{ yr}^{-1}$ ), Laptev Sea ( $\langle K_{\text{region}} \rangle \approx 0.03 \text{ yr}^{-1}$ ), and Kara Sea  
373 ( $\langle K_{\text{region}} \rangle \approx 0.01 \text{ yr}^{-1}$ )), due to shallower water depths and high OM fluxes from inland  
374 (Burwicz et al., 2011; Seiter et al., 2004). Besides that, the global map also highlights the  
375 extremely low OM reactivity, especially in some regions, as indicated by the absence of  
376 sulfate-methane transition (SMT) (e.g., the NE-Pacific, NEPAC) (Eggert et al., 2018) and  
377 central ocean gyre regions (e.g., South Pacific Gyre) (LaRowe et al., 2020b). Deeper water  
378 depth (>5000m), relatively low OM content (~0.2wt.%), and the old OM age (>10<sup>4</sup> years)  
379 result in comparably lower  $\mu$  and  $\sigma$  values (Fig.9A and 9B) and, thus, extremely low benthic  
380 OM reactivity ( $\langle K_{\text{region}} \rangle \approx 10^{-4} \text{ yr}^{-1}$ ) (Kallmeyer et al., 2012, Müller and Suess, 1979).  
381 Normally, greater water depth enhances oxygen exposure time for OM degradation, and  
382 thereby reduce the reactivity of OM arriving at the seafloor, as reflected in the smaller  $\mu$   
383 values (Fig. 9A). In ocean areas characterized by pronounced OMZs, however, due to  
384 strong coastal upwelling or a high export rate of plankton-derived OM, the inhibition of  
385 OM degradation processes in the water column results in the preservation of

386 heterogeneously mixed OM components (both active and refractory), as reflected in the  
387 larger  $\sigma$  values (Fig. 9B), leading to higher than expected OM reactivity in specific regions  
388 despite greater water depths (e.g., ARBS and EWTP ( $\langle K_{\text{region}} \rangle \approx 0.01 \text{ yr}^{-1}$ ) (Fig. 9C). Thus,  
389 the *l*-RCM provides a new framework not only for identifying the differences in OM  
390 reactivity between regions, but also for assessing regional/global OM reactivity patterns  
391 using easily obtainable information (e.g., sedimentation).

392 OM reactivity exerts an important control on the relative significance of OM degradation  
393 pathways in marine sediments. In oxic environments, OM will be mainly respired  
394 aerobically and through denitrification, whereas deeper within the sediment, it will mainly  
395 be decomposed through anaerobic pathways such as sulfate reduction and methanogenesis  
396 (Regnier et al., 2011). Therefore, further work should be conducted to simulate the  
397 associated biogeochemical processes using the *l*-RCM to better quantify OM degradation  
398 and burial in marine sediments on regional or global scales.

399



400

401 **Figure 9. Distribution of  $\mu$  (A),  $\sigma$  (B), and  $\langle k \rangle$  (C) in the global ocean with  $1^\circ \times 1^\circ$**   
 402 **resolution.**

403

404 **Table 2. Abbreviations of regions in this paper (Seiter et al., 2004), and their area,**  
 405 **mean water depth, mean OM content in surface sediment (<5 cm), and apparent OM**  
 406 **degradation rata ( $\langle K_{\text{region}} \rangle$ ).**

Abbreviation	Region	water depth <sup>a</sup> (m)	Mean OM (wt.%)	$\langle K_{\text{region}} \rangle$ (yr <sup>-1</sup> )
SWAF	SW-Africa continental margin	334	2.5	0.48542
NWAM	NW-America continental margin	731	1.7	0.12695
ARBS	Arabian Sea	1600	1.4	0.08182
EWTP	East-West Coastal Equatorial Pacific	3662	1.2	0.01587
ANT	South Polar Sea	1300	0.3	0.00029
ARGCO	Argentina continental margin	1859	0.3	0.00026
BARENTKAR	Barents Sea and Kara Sea	224	1.1	0.02081
BRAZCO	Brazil continental margin	1051	0.5	0.00034
CANAR	Canaries	1190	0.6	0.00031
CEPAC	Central Equatorial Pacific	5022	0.3	0.00002
CHICO	Chile continental margin	1444	1.5	0.00028
ETROPAT	Eastern tropical Atlantic	2253	0.7	0.00026
EUR1	N-European continental margin	1290	0.8	0.00029
EUR2	S-European continental margin	974	0.3	0.00037
GROE	Northern Nordic Sea	1563	0.7	0.00027
GUBRACO	SE-America continental margin	1844	0.4	0.00026
GUI	Gulf of Guinea	1586	1.1	0.00027
INA	Indian Ocean deep sea	4042	0.4	0.00021
KARA2	Kara Sea	281	1.2	0.01111
LAPTEVSEA	Laptev Sea	190	0.9	0.02964
NEAM	NE-America continental margin	1045	0.9	0.00034
NEPAC	NE-Pacific	4463	0.4	0.00012
NOATL	Northern Atlantic	2161	0.4	0.00026
NWPAC	NW-Pacific	4898	0.6	0.00004
PERCO	Peru continental margin	1020	4.8	0.00035
RIOPLATA	Rio de la Plata mouth	1784	0.8	0.00026
SEPAC	SE-Pacific	3952	0.5	0.00022
SOATL	Southern Atlantic	3592	0.4	0.00024
SWPAC	SW-Pacific	3153	0.8	0.00025
WAFCO	W-Africa continental margin	1982	0.6	0.00026

407 <sup>a</sup>water depth and mean OM content are based on the average depth and OM content of the  
 408 sites in each region of Fig.4.

409

## 410 **4 Conclusions**

411 Compared with previous OM degradation models, the *l*-RCM presented here not only  
412 well fits OM depth-content profiles, but also better represents the distribution of OM  
413 reactivity by the parameters  $\mu$  and  $\sigma$ . We use the *l*-RCM to inversely determine  $\mu$  and  $\sigma$  at  
414 123 sites across the global ocean, including shelf, slope, and abyssal regions. Our results  
415 show that the apparent OM reactivity ( $\langle k \rangle = \mu \cdot \exp(\sigma^2/2)$ ) decreases with decreasing  
416 sedimentation rate ( $\omega$ ), and that OM reactivity is more than three orders of magnitude  
417 higher in shelf than in abyssal regions. Due to the complex depositional environments (e.g.,  
418 oxygen minimum zones), OM reactivity is higher than predicted in some specific regions  
419 (e.g., the NWAM, SWAF, ARBS, and EWTP), which was also captured by the *l*-RCM in  
420 these regions. Based on two empirical relationships of  $\langle k \rangle$  with  $\omega$  and  $\omega$  with  $z$ , we  
421 obtained the global OM reactivity distribution patterns and finally mapped the global OM  
422 reactivity distribution.

423 The reactivity of OM serving as fuel for microbial activity in marine sediments firmly  
424 controls the degradation pathways and metabolism rates. Thus, the *l*-RCM has direct  
425 implications on the constraints for OM degradation and burial in marine sediments on  
426 regional or global scales.

427

## 428 **References**

- 429 Aller, R. C.: Bioturbation and remineralization of sedimentary organic matter: effects of  
430 redox oscillation, *Chem Geol*, 114, 331-345, doi:10.1016/0009-2541(94)90062-0,  
431 1994.
- 432 Aris, R.: Prolegomena to the rational analysis of systems of chemical reactions II. Some  
433 addenda, *Archive for Rational Mechanics and Analysis*, 27, 356-364,  
434 doi:10.1007/BF00282276, 1968.
- 435 Arndt, S., Jørgensen, B. B., LaRowe, D. E., Middelburg, J., Pancost, R., and Regnier, P.:  
436 Quantifying the degradation of organic matter in marine sediments: a review and  
437 synthesis, *Earth-science reviews*, 123, 53-86, doi:10.1016/j.earscirev.2013.02.008,  
438 2013.



439 Berg, P., Rysgaard, S., Thamdrup, B.,: Dynamic modeling of early diagenesis and nutrient  
440 cycling. A case study in an Arctic marine sediment, *American Journal of Science* 303,  
441 905–955, doi: 10.2475/ajs.303.10.905, 2003.

442 Berner, R. A.: An idealized model of dissolved sulfate distribution in recent sediments,  
443 *Geochimica et Cosmochimica Acta*, 28, 1497-1503, doi:10.1016/0016-7037(64)90164-  
444 4, 1964.

445 Bogus, K. A., Zonneveld, K. A., Fischer, D., Kasten, S., Bohrmann, G., and Versteegh, G.  
446 J.: The effect of meter-scale lateral oxygen gradients at the sediment-water interface on  
447 selected organic matter based alteration, productivity and temperature proxies,  
448 *Biogeosciences*, 9, 1553-1570, doi:10.5194/bg-9-1553-2012, 2012.

449 Boudreau, B. P.: A kinetic model for microbial organic-matter decomposition in marine  
450 sediments, *FEMS microbiology ecology*, 11, 1-14, doi:10.1111/j.1574-  
451 6968.1992.tb05789.x, 1992.

452 Boudreau, B. P.: A method-of-lines code for carbon and nutrient diagenesis in aquatic  
453 sediments, *Computers & Geosciences*, 22, 479-496, doi:10.1016/0098-  
454 3004(95)00115-8, 1996.

455 Boudreau, B. P., Arnosti, C., Jørgensen, B. B., and Canfield, D. E.: Comment on " Physical  
456 model for the decay and preservation of marine organic carbon", *Science*, 319(5870),  
457 1616-1616, doi:10.1126/science.1148589, 2008.

458 Boudreau, B. P. and Ruddick, B. R.: On a reactive continuum representation of organic  
459 matter diagenesis, *American Journal of Science*, 291, 507-538,  
460 doi:10.2475/ajs.291.5.507, 1991.

461 Bradley, J., Arndt, S., Amend, J., Burwicz, E., Dale, A. W., Egger, M., and LaRowe, D.  
462 E.: Widespread energy limitation to life in global subseafloor sediments, *Science*  
463 *advances*, 6, doi:10.1126/sciadv.aba0697, 2020.

464 Burdige, D. J.: Preservation of organic matter in marine sediments: controls, mechanisms,  
465 and an imbalance in sediment organic carbon budgets?, *Chem Rev*, 107, 467-485,  
466 doi:10.1021/cr050347q, 2007.

467 Burwicz, E. B., Rüpke, L., and Wallmann, K.: Estimation of the global amount of  
468 submarine gas hydrates formed via microbial methane formation based on numerical  
469 reaction-transport modeling and a novel parameterization of Holocene sedimentation,  
470 *Geochimica et Cosmochimica Acta*, 75, 4562-4576, doi:10.1016/j.gca.2011.05.029,  
471 2011.

472 Cael, B., Bisson, K., and Follett, C. L.: Can rates of ocean primary production and  
473 biological carbon export be related through their probability distributions?, *Global*  
474 *biogeochemical cycles*, 32, 954-970, doi:10.1029/2017GB005797, 2018.

475 Dickens, A. F., Gelinas, Y., Masiello, C. A., Wakeham, S., and Hedges, J. I.: Reburial of  
476 fossil organic carbon in marine sediments, *Nature*, 427, 336-339,  
477 doi:10.1038/nature02299, 2004.

478 Dunne, J. P., Sarmiento, J. L., and Gnanadesikan, A.: A synthesis of global particle export  
479 from the surface ocean and cycling through the ocean interior and on the seafloor, *Global*  
480 *Biogeochemical Cycles*, 21, doi:10.1029/2006GB002907, 2007.

481 Egger, M., Riedinger, N., Mogollón, J. M., and Jørgensen, B. B.: Global diffusive fluxes  
482 of methane in marine sediments, *Nature Geoscience*, 11, 421-425,  
483 doi:10.1038/s41561-018-0122-8, 2018.

484 Forney, D. and Rothman, D.: Inverse method for estimating respiration rates from decay  
485 time series, *Biogeosciences*, 9, 3601-3612, doi:10.5194/bg-9-3601-2012, 2012a.  
486 Forney, D. C. and Rothman, D. H.: Common structure in the heterogeneity of plant-matter  
487 decay, *Journal of The Royal Society Interface*, 9, 2255-2267,  
488 doi:10.1098/rsif.2012.0122, 2012b.  
489 Forney, D. C., and Rothman, D. H.: Carbon transit through degradation networks,  
490 *Ecological Monographs*, 84(1), 109-129, doi: 10.1890/12-1846.1, 2014.  
491 Freitas, F. S., Pika, P. A., Kasten, S., Jørgensen, B. B., Rassmann, J., Rabouille, C.,  
492 Thomas, S., Sass, H., Pancost, R. D., and Arndt, S.: Advancing on large-scale trends of  
493 apparent organic matter reactivity in marine sediments and patterns of benthic carbon  
494 transformation, *Biogeosciences Discussions*, 2021, 1-64, doi:10.5194/bg-18-4651-2021,  
495 2021.  
496 Garber, J. H.: Laboratory study of nitrogen and phosphorus remineralization during the  
497 decomposition of coastal plankton and seston, *Estuarine, Coastal and Shelf Science*, 18,  
498 685-702, doi:10.1016/0272-7714(84)90039-8, 1984.  
499 Griffith, D. R., Martin, W. R., and Eglinton, T. I.: The radiocarbon age of organic carbon  
500 in marine surface sediments. *Geochimica et Cosmochimica Acta*, 74(23), 6788-6800,  
501 doi:10.1016/j.gca.2010.09.001, 2010.  
502 Hammond, D., McManus, J., Berelson, W., Kilgore, T., and Pope, R.: Early diagenesis of  
503 organic material in equatorial Pacific sediments: stoichiometry and kinetics, *Deep Sea*  
504 *Research Part II: Topical Studies in Oceanography*, 43, 1365-1412, doi:10.1016/0967-  
505 0645(96)00027-6, 1996.  
506 Hartnett, H. E., Keil, R. G., Hedges, J. I., and Devol, A. H.: Influence of oxygen exposure  
507 time on organic carbon preservation in continental margin sediments, *Nature*,  
508 391(6667), 572-575, doi:10.1038/35351, 1998.  
509 Hedges, J. I. and Keil, R. G.: Sedimentary organic matter preservation: an assessment and  
510 speculative synthesis, *Marine chemistry*, 49, 81-115, doi:10.1016/0304-4203(95)00008-  
511 F, 1995.  
512 Hewson, I., Barbosa, J. G., Brown, J. M., Donelan, R. P., Eaglesham, J. B., Eggleston, E.  
513 M., and LaBarre, B. A.: Temporal dynamics and decay of putatively allochthonous and  
514 autochthonous viral genotypes in contrasting freshwater lakes, *Applied and*  
515 *environmental microbiology*, 78, 6583-6591, doi:10.1128/AEM.01705-12, 2012.  
516 Ho, T. and Aris, R.: On apparent second-order kinetics, *AIChE journal*, 33, 1050-1051,  
517 doi:10.1002/aic.690330621, 1987.  
518 Ingole, B. S., Sautya, S., Sivadas, S., Singh, R., and Nanajkar, M.: Macrofaunal community  
519 structure in the western Indian continental margin including the oxygen minimum zone,  
520 *Marine Ecology*, 31, 148-166, doi:10.1111/j.1439-0485.2009.00356.x, 2010.  
521 Jørgensen, B.: A comparison of methods for the quantification of bacterial sulfate reduction  
522 in coastal marine sediments. II. Calculation from mathematical models, *Geomicrobiol.*  
523 *J*, 1, 29-47, doi:10.1080/01490457809377721, 1978.  
524 Jørgensen, B.: Processes at the sediment-water interface, *The major biogeochemical cycles*  
525 *and their interactions*, 477-509, 1983.  
526 Jørgensen, B. B., Wenzhöfer, F., Egger, M., and Glud, R. N.: Sediment oxygen  
527 consumption: Role in the global marine carbon cycle, *Earth-science reviews*, 228,  
528 103987. doi:10.1016/j.earscirev.2022.103987, 2022.

529 Kallmeyer, J., Pockalny, R., Adhikari, R. R., Smith, D. C., and D'Hondt, S.: Global  
530 distribution of microbial abundance and biomass in subseafloor sediment,  
531 Proceedings of the National Academy of Sciences, 109(40), 16213-16216, doi:  
532 10.1073/pnas.1203849109, 2012.

533 Katsev, S. and Crowe, S. A.: Organic carbon burial efficiencies in sediments: The power  
534 law of mineralization revisited, *Geology*, 43, 607-610, doi:10.1130/G36626.1, 2015.

535 Krumins, V., Gehlen, M., Arndt, S., Van Cappellen, P., and Regnier, P.: Dissolved  
536 inorganic carbon and alkalinity fluxes from coastal marine sediments: model estimates  
537 for different shelf environments and sensitivity to global change, *Biogeosciences*, 10,  
538 371-398, doi:10.5194/bg-10-371-2013, 2013.

539 LaRowe, D., Arndt, S., Bradley, J., Estes, E., Hoarfrost, A., Lang, S., Lloyd, K.,  
540 Mahmoudi, N., Orsi, W., and Walter, S. S.: The fate of organic carbon in marine  
541 sediments-New insights from recent data and analysis, *Earth-Science Reviews*, 204,  
542 103146, doi:10.1016/j.earscirev.2020.103146, 2020a.

543 LaRowe, D. E., Arndt, S., Bradley, J. A., Burwicz, E., Dale, A. W., and Amend, J. P.:  
544 Organic carbon and microbial activity in marine sediments on a global scale throughout  
545 the Quaternary, *Geochimica et Cosmochimica Acta*, 286, 227-247,  
546 doi:10.1016/j.gca.2020.07.017, 2020b.

547 Limpert, E., Stahel, W. A., and Abbt, M.: Log-normal distributions across the sciences:  
548 keys and clues: on the charms of statistics, and how mechanical models resembling  
549 gambling machines offer a link to a handy way to characterize log-normal distributions,  
550 which can provide deeper insight into variability and probability—normal or log-  
551 normal: that is the question, *BioScience*, 51, 341-352, doi:10.1641/0006-  
552 3568(2001)051[0341:LNDATS]2.0.CO;2, 2001.

553 Luff, R., Wallmann, K., and Aloisi, G.: Numerical modeling of carbonate crust formation  
554 at cold vent sites: significance for fluid and methane budgets and chemosynthetic  
555 biological communities. *Earth and Planetary Science Letters*, 221, 1-4, 337-353. doi:  
556 10.1016/S0012-821X(04)00107-4, 2004.

557 Luff, R., Wallmann, K., Grandel, S., and Schlüter, M.: Numerical modeling of benthic  
558 processes in the deep Arabian Sea, *Deep Sea Research Part II: Topical Studies in*  
559 *Oceanography*, 47, 3039-3072, doi:10.1016/S0967-0645(00)00058-8, 2000.

560 Meister, P., Herda, G., Petrishcheva, E., Gier, S., Dickens, G. R., Bauer, C., and Liu, B.:  
561 Microbial alkalinity production and silicate alteration in methane charged marine  
562 sediments: Implications for porewater chemistry and diagenetic carbonate formation,  
563 *Frontiers in Earth Science*, 9: 756591, doi:10.3389/feart.2021.756591, 2022.

564 Meysman, F. J., Middelburg, J. J., Herman, P. M., and Heip, C. H.: Reactive transport in  
565 surface sediments. II. Media: an object-oriented problem-solving environment for early  
566 diagenesis, *Computers & geosciences*, 29, 301-318, doi:10.1016/S0098-  
567 3004(03)00007-4, 2003.

568 Middelburg, J. J.: A simple rate model for organic matter decomposition in marine  
569 sediments, *Geochimica et Cosmochimica acta*, 53, 1577-1581, 10.1016/0016-  
570 7037(89)90239-1, doi:10.1016/0016-7037(89)90239-1, 1989.

571 Middelburg, J. J., Soetaert, K., and Herman, P. M.: Empirical relationships for use in global  
572 diagenetic models, *Deep Sea Research Part I: Oceanographic Research Papers*, 44, 327-  
573 344, doi:10.1016/S0967-0637(96)00101-X, 1997.

574 Mollenhauer, G., Eglinton, T. I., Ohkouchi, N., Schneider, R. R., Müller, P. J., Grootes, P.  
575 M., and Rullkötter, J.: Asynchronous alkenone and foraminifera records from the  
576 Benguela Upwelling System, *Geochimica et cosmochimica acta*, 67, 2157-2171,  
577 doi:10.1016/S0016-7037(03)00168-6, 2003.

578 Müller, P. J. and Suess, E.: Productivity, sedimentation rate, and sedimentary organic  
579 matter in the oceans—I. Organic carbon preservation, *Deep Sea Research Part A.*  
580 *Oceanographic Research Papers*, 26, 1347-1362, doi:10.1016/0198-0149(79)90003-7,  
581 1979.

582 Munhoven, G.: Glacial–interglacial rain ratio changes: Implications for atmospheric CO<sub>2</sub>  
583 and ocean–sediment interaction, *Deep Sea Research Part II: Topical Studies in*  
584 *Oceanography*, 54, 722-746, doi:10.1016/j.dsr2.2007.01.008, 2007.

585 Nöthen, K., Kasten, S.: Reconstructing changes in seep activity by means of pore water  
586 and solid phase Sr/Ca and Mg/Ca ratios in pockmark sediments of the Northern Congo  
587 Fan, *Marine Geology*, 287(1-4): 1-13, doi:10.1016/j.margeo.2011.06.008, 2011.

588 Pika, P., Hülse, D., and Arndt, S.: OMEN-SED (-RCM)(v1. 1): a pseudo-reactive  
589 continuum representation of organic matter degradation dynamics for OMEN-SED,  
590 *Geoscientific Model Development*, 14, 7155-7174, doi:10.5194/gmd-14-7155-2021,  
591 2021.

592 Regnier, P., Dale, A. W., Arndt, S., LaRowe, D. E., Mogollón, J., and Van Cappellen, P.:  
593 Quantitative analysis of anaerobic oxidation of methane (AOM) in marine sediments: A  
594 modeling perspective, *Earth-Science Reviews*, 106(1-2), 105-130,  
595 doi:10.1016/j.earscirev.2011.01.002, 2011.

596 Rowe, G. T. and Staresinic, N.: Sources of organic matter to the deep-sea benthos, *Ambio*  
597 *Special Report*, 19-23, doi:10.2307/25099603, 1979.

598 Seiter, K., Hensen, C., Schröter, J., and Zabel, M.: Organic carbon content in surface  
599 sediments—defining regional provinces, *Deep Sea Research Part I: Oceanographic*  
600 *Research Papers*, 51, 2001-2026, doi:10.1016/j.dsr.2004.06.014, 2004.

601 Smith, S. and Hollibaugh, J.: Coastal metabolism and the oceanic organic carbon balance,  
602 *Reviews of Geophysics*, 31, 75-89, doi:10.1029/92RG02584, 1993.

603 Volz, J. B., Mogollón, J. M., Geibert, W., Arbizu, P. M., Koschinsky, A., and Kasten, S.:  
604 Natural spatial variability of depositional conditions, biogeochemical processes and  
605 element fluxes in sediments of the eastern Clarion-Clipperton Zone, Pacific Ocean, *Deep*  
606 *Sea Research Part I: Oceanographic Research Papers*, 140, 159-172,  
607 doi:10.1016/j.dsr.2018.08.006, 2018.

608 Westrich, J. T. and Berner, R. A.: The role of sedimentary organic matter in bacterial  
609 sulfate reduction: The G model tested 1, *Limnology and oceanography*, 29, 236-249,  
610 doi:10.4319/lo.1984.29.2.0236, 1984.

611 Whiticar, M. J.: Carbon and hydrogen isotope systematics of bacterial formation and  
612 oxidation of methane. *Chemical geology*, 161, 291–314. doi: 10.1016/S0009-  
613 2541(99)00092-3, 1999.

614 Zonneveld, K. A., Versteegh, G. J., Kasten, S., Eglinton, T. I., Emeis, K.-C., Huguet, C.,  
615 Koch, B. P., de Lange, G. J., de Leeuw, J. W., and Middelburg, J. J.: Selective  
616 preservation of organic matter in marine environments; processes and impact on the  
617 sedimentary record, *Biogeosciences*, 7, 483-511, doi:10.5194/bg-7-483-2010, 2010.

618

619 **Acknowledges**

620 This study was supported by National Key Basic Research and Development Program of  
621 China (2022YFC2805400; 2016YFA0601100), the Natural Science Foundation of China  
622 (41976057; 42276059). Sinan Xu gratefully acknowledges the financial support by the  
623 China Scholarship Council (contract N. 201906260048) for a research stay at AWI,  
624 Germany. Bo Liu and Sabine Kasten acknowledge the BMBF MARE: N project  
625 “Anthropogenic impacts on particulate organic carbon cycling in the North Sea (APOC)”  
626 (03F0874A).

627 **Author contributions**

628 S.X. and B.L. designed the study and performed the research with S.A., S.K., and Z.W.;

629 All authors discussed the results and commented on the manuscript.

630 **Competing interests**

631 The authors declare that they have no competing interests.